



Waveform Energy Focusing Tomography With Passive Seismic Sources

Yueqiao Hu¹, Junlun Li^{1,2*} and Haijiang Zhang^{1,2}

¹Laboratory of Seismology and Physics of Earth's Interior, School of Earth and Space Sciences, University of Science and Technology of China, Hefei, China, ²Mengcheng National Geophysical Observatory, University of Science and Technology of China, Hefei, China

OPEN ACCESS

Edited by:

Tariq Alkhalifah,
King Abdullah University of Science
and Technology, Saudi Arabia

Reviewed by:

Hanchen Wang,
Los Alamos National Laboratory
(DOE), United States
Denis Anikiev,
GFZ German Research Centre for
Geosciences, Germany

*Correspondence:

Junlun Li
lijunlun@ustc.edu.cn

Specialty section:

This article was submitted to
Solid Earth Geophysics,
a section of the journal
Frontiers in Earth Science

Received: 20 March 2022

Accepted: 09 May 2022

Published: 13 June 2022

Citation:

Hu Y, Li J and Zhang H (2022)
Waveform Energy Focusing
Tomography With Passive
Seismic Sources.
Front. Earth Sci. 10:900435.
doi: 10.3389/feart.2022.900435

By taking advantage of the information carried by the entire seismic wavefield, Full Waveform Inversion (FWI) is able to yield higher resolution subsurface velocity models than seismic traveltimes tomography. However, FWI heavily relies on the knowledge of source information and good initial models, and could be easily trapped into local minima caused by cycle skipping issue because of its high nonlinearity. To mitigate these issues in FWI, we propose a novel method called Waveform Energy Focusing Tomography (WEFT) for passive seismic sources. Unlike conventional FWI, WEFT back-propagates the seismic records directly instead of the data residuals, and updates the velocity models by maximizing the stacking energy for all the moment tensor components from back-propagated wavefields around the sources. Therefore, except for source locations and origin times, WEFT does not require other source attributes in advance for the inversion. Since WEFT does not aim at fitting synthetic and observed waveforms, it has lower nonlinearity and is less prone to the cycle skipping issue compared to FWI. For the proof of concept, we have validated WEFT using several 2D synthetic tests to show it is less affected by inaccurate source locations and data noise. These advantages render WEFT more applicable for tomography using passive seismic sources when the source information is generally not accurately known. Although the inverted model from WEFT is inevitably influenced by the source distribution as well as its radiation patterns, and its resolution is likely lower than that of FWI, it can act as an intermediate step between traveltimes tomography and FWI by providing a more reliable and accurate velocity model for the latter.

Keywords: waveform tomography, passive seismic sources, energy focusing, seismic moment tensor, time-reversal method

INTRODUCTION

Seismic tomography is an essential approach for imaging the subsurface structure. The well-established seismic traveltimes tomographic methods based on ray theory have had many successful applications in imaging structures at different scales in the past few decades (e.g., Bording et al., 1987; Lanz et al., 1998; Rawlinson and Sambridge, 2003; Zhang and Thurber, 2003). More recently, Full Waveform Inversion (FWI) has also been developed and applied at many different scales (Ravaut et al., 2004; Bleibinhaus et al., 2007; Fichtner et al., 2013; Adamczyk et al., 2015; Bozdağ et al., 2016), as it can potentially obtain models with higher resolution by using more information carried in the waveforms (Virieux and Operto, 2009; Alkhalifah, 2014).

Traditional FWI inverts for subsurface velocities by minimizing the L2-norm misfit between the observed and simulated seismic waveforms (Tarantola, 1984; Pratt and Worthington, 1990). In spite of some successful applications on both active and passive seismic data (Brenders and Pratt, 2007; Fichtner et al., 2009, 2013; Tape et al., 2009, 2010; Warner et al., 2013; Operto et al., 2015), there are still practical issues and challenges yet to be solved in FWI. One of the critical issues is that FWI tends to fall into local minima when the time delay between the synthetic and observed waveforms is larger than half a cycle due to inaccurate starting velocity models, which is referred to as the cycle skipping (Virieux and Operto, 2009). Many efforts have been devoted to solving this problem from different aspects. For example, the multiscale strategy (Bunks et al., 1995; Sirgue and Pratt, 2004), which sequentially performs inversion from lower to higher frequencies, can efficiently avoid cycle skipping since waveforms at lower frequencies have broader cycles. Shin and Cha (2008), Shin and Cha (2009) extended the time-domain FWI to the Laplace-domain and Laplace-Fourier domain to build long-wavelength velocity models and increase the stability of the inversion. Choi and Alkhalifah (2015) developed the unwrapped phase inversion combined with exponential damping, which can avoid cycle-based jumps even when low-frequency information is missing.

Since the objective function based on the L2-norm often has stronger nonconvexity, a variety of misfit functionals have been proposed to measure the discrepancies between the observed and synthetic waveforms. The cross-correlation based objective functions (e.g., Luo and Schuster, 1991; van Leeuwen and Mulder, 2010) were proposed to measure the similarity between the observed and synthetic data, which are more dependent on the waveform kinematics and thus mitigate issues related to amplitudes. Although these objective functions are less susceptible to cycle skipping, a band-limited or non-impulsive source function may still affect the measurement of waveform discrepancies. The deconvolution-based objective function (Luo and Sava 2011) is thus proposed to alleviate the issue. The misfit measured by the discrepancy in waveform envelopes can be used to retrieve the long-wavelength component of a velocity model, and thus reduce the dependence of FWI on the initial model (Bozdağ et al., 2011; Wu et al., 2014; Luo and Wu, 2015; Oh and Alkhalifah, 2018). In addition, the misfit functions based on the optimal transport provide an alternative in an attempt to overcome the cycle skipping issue (Engquist and Froese, 2013; Métivier et al., 2016; Yang and Engquist, 2018). Recently, the new methods related to non-physical model extensions, such as reconstructed wavefields (van Leeuwen and Herrmann, 2013; Wang et al., 2016; Alkhalifah and Song, 2019), time lag extension (Yang and Sava, 2013; Biondi and Almomin, 2014), and matching filter (Luo and Sava, 2011; Warner and Guasch, 2016; Huang et al., 2017; Sun and Alkhalifah, 2019; Li and Alkhalifah, 2021) are also attractive for their stronger resistance to cycle skipping.

The source information is essential for FWI when calculating the synthetic waveforms, which is oftentimes inaccurate or even unknown. For an active seismic survey, though the source wavelet (or source time function) can be extracted directly from the near-

offset traces (Schuster, 2017), the extraction is often successful only for data with high signal-to-noise ratios (SNRs). Owing to the linear relationship between the source attributes and the seismic data, the source wavelet can be obtained by solving a linear equation by assuming a relatively accurate velocity model is available (Pratt, 1999). Additionally, several strategies were also proposed to remove the influence of source wavelet based on convolution (Choi et al., 2005; Cheong et al., 2006; Choi and Alkhalifah, 2011; Wang and Alkhalifah, 2018; Wang et al., 2020) or deconvolution (Lee and Kim, 2003; Xu et al., 2006) of reference traces in both time and frequency domains. However, it may not be a trivial task to choose a reference trace for real-data applications.

In addition to the source time function, for passive seismic sources, the source moment tensor is also needed for FWI. Using the information from first motion polarities (e.g., Rau et al., 1996; Hardebeck and Shearer 2002), and/or the S/P amplitude ratios (Julian et al., 1998; Hardebeck and Shearer, 2003), to full waveforms (Li et al., 2011; Zhu and Ben-Zion, 2013; Willacy et al., 2019), source moment tensors can be characterized with increasing reliability. However, the inversion process inevitably becomes more computationally expensive and more complicated, and it generally requires a more accurate velocity model (Kim et al., 2011; Eyre and van der Baan, 2015). When the surface seismic acquisition array is dense, Time Reversal (TR) methods (Larmat et al., 2006; Kawakatsu and Montagner, 2008; Artman et al., 2010; Gharti et al., 2011; Chambers et al., 2014; Nakata and Beroza, 2016; Sun et al., 2016) based on seismic migration can be used to image the source attributes directly by back-propagating the observed data. For instance, for the microseismic datasets which have relatively lower SNR, not only phase picking is avoided, but also the influence of noise can be mitigated by stacking the back-propagated wavefields from many individual receivers with the TR methods (Gharti et al., 2011). However, the source attributes may not be well reconstructed if the observation array cannot record a sufficient amount of wavefield information from the source (Bazargani and Snieder, 2016). Furthermore, methods based on the machine learning, which demand less processing effort and computational costs, have become more appealing for obtaining the information of passive seismic sources (Kriegerowski et al., 2019; van den Ende and Ampuero, 2020; Wang and Alkhalifah, 2021; Smith et al., 2022). The seismic moment tensor can be determined according to the first-motion polarities picked by deep learning (Ross et al., 2018; Hara et al., 2019; Uchide, 2020). Kuang et al. (2021) proposed the Focal Mechanism Network (FMNet) to determine the seismic moment tensor directly from seismic waveforms. Based on the Bayesian Neural Networks (BNNs), Steinberg et al. (2021) estimated the moment tensor of earthquakes as well as parameter uncertainties. Although the machine-learning based methods can efficiently estimate source mechanisms, those methods are still limited by predefined Earth models and station distributions used for training the neural networks.

In order to overcome the aforementioned problems, many methods have been developed to invert for the velocity models with passive seismic sources. Using the variable projection

method, Sun et al. (2016) developed a framework of joint full-waveform inversion to obtain velocity models and passive seismic source locations simultaneously. Song et al. (2019a) proposed an objective function to invert for velocities and estimate source locations together by penalizing source energy away from the source location. Based on the geometric-mean imaging condition (Nakata and Beroza, 2016), Lyu and Nakata (2020) performed passive-source location and velocity inversion using FWI iteratively. However, these methods failed to consider the influence of the source radiation pattern, and corresponding FWI schemes still have high nonlinearity. By focusing different modes (PP, SS and PS) of the source images, a variety of methods for determining source locations as well as velocity models (Vp, Vs.) (Witten and Shragge, 2017; Rocha et al., 2019; Oren and Shragge, 2021; Oren and Shragge, 2022) have been developed using different imaging conditions. Since modeling elastic wavefields (both P- and S wave) is necessary for these methods, the computational cost is rather demanding, especially for 3D cases. Inspired by the TR principle, Lellouch and Landa (2018) used a minimum variation criterion to evaluate the coherency among focused sources and estimated the velocity model. Nevertheless, the influence of the source radiation pattern from different source mechanisms was still ignored, and trace normalization was used instead to mitigate the source effect.

For seismic exploration data using active seismic sources, to mitigate the aforementioned challenges in FWI, Zhang and Wang (2009) proposed a new method implemented in the tau-p domain by maximizing the stacking energy of the back-propagated wavefield at the source locations. Jin and Plessix (2013) further modified this method and used a volume centered at the source position instead of a single grid point for energy stacking in the data domain. Though the dependence on waveform fitting and the initial model is largely relaxed with the energy stacking approach, their methods were designed for active sources and are not directly applicable for earthquake sources with distinct source radiation patterns, which emanate waves with varying amplitudes and polarities in different directions.

In this study, we further extend the method of Jin and Plessix (2013) to passive sources. Since the locations of passive seismic sources and accompanying 1D layered structures (Kissling et al., 1995) or full 3D velocity models (Thurber, 1992) can be determined simultaneously using arrival times picked manually or automatically, we assume that the rough source locations are known a priori in this study while the uncertainties are also taken into consideration. The new method inverts for the velocity model by maximizing the spatiotemporally stacking energy for all the moment time functions from the back-propagated wavefields around the source location over a short time window and a limited volume, and the source attributes except for the rough source locations are therefore not required in advance. A multiscale strategy is also applied to stabilize the inversion. We will first present the newly proposed method and then validate the method with several numerical examples in two dimensions for simplicity.

WAVEFORM ENERGY FOCUSING TOMOGRAPHY FOR PASSIVE SEISMIC SOURCES

Based on the reversibility of wave propagation through simulation means, the time-reversal technique can refocus the back-propagated wavefields and maximize the stacking energy at the source location and origin time if the velocity model is correct (McMechan, 1982; Fink, 1997). Therefore, the amount of energy focused around the source can be used as the criterion for optimizing a velocity model when the source location is roughly known (Zhang and Wang, 2009; Jin and Plessix, 2013). For passive seismic sources, we measure the stacking energy for all the moment time functions from back-propagated wavefields. For simplicity, we first propose the method based on the 2D observation geometry in this study. The corresponding objective function in 2D is

$$E(v) = -\frac{1}{2} \int_{\tilde{t}_0}^{t_{max}} \left(\hat{M}_{xx}^{TR^2}(\xi, t) + \hat{M}_{xz}^{TR^2}(\xi, t) + \hat{M}_{zx}^{TR^2}(\xi, t) + \hat{M}_{zz}^{TR^2}(\xi, t) \right) dt \quad (1)$$

where $\hat{M}_{ij}^{TR}(\xi, t)$ denotes the moment tensor components estimated from the back-propagated wavefields at the source location ξ , and $\hat{M}_{ij}^{TR^2}(\xi, t)$ denotes the stacking energy. The \tilde{t}_0 and t_{max} define the time duration for stacking. With a negative sign, the criterion is to minimize the negative of the stacking energy.

With the time-reversal imaging (TRI), $\hat{M}_{ij}^{TR}(\xi, t)$ can be estimated by (Kawakatsu and Montagner, 2008)

$$\hat{M}_{ij}^{TR}(\xi, t) = E_{ijn}(\xi, t; \mathbf{x}_r, 0) * u_n(\mathbf{x}_r, -t) \quad (2)$$

where $u_n(\mathbf{x}_r, -t)$ is the n th component of time-reversed version of the observed displacement at the receiver location \mathbf{x}_r , the symbol $*$ denotes convolution, and E_{ijn} is the strain Green's tensor defined as

$$E_{ijn}(\xi, t; \mathbf{x}_r, 0) = c_{ij} \left(\frac{\partial G_{in}(\xi, t; \mathbf{x}_r, 0)}{\partial \xi_j} + \frac{\partial G_{jn}(\xi, t; \mathbf{x}_r, 0)}{\partial \xi_i} \right) \quad (3)$$

in which $c_{ij} = 1/2$ for $i = j$ and $c_{ij} = 1$ otherwise. Thus, **Equation 2** can be rewritten as

$$\hat{M}_{ij}^{TR}(\xi, t) = \begin{cases} \frac{\partial G_{in}(\xi, t; \mathbf{x}_r, 0)}{\partial \xi_i} * u_n(\mathbf{x}_r, -t), & i = j \\ \left(\frac{\partial G_{in}(\xi, t; \mathbf{x}_r, 0)}{\partial \xi_j} + \frac{\partial G_{jn}(\xi, t; \mathbf{x}_r, 0)}{\partial \xi_i} \right) * u_n(\mathbf{x}_r, -t), & i \neq j \end{cases} \quad (4)$$

Using the relationship with differentiation, the estimated moment tensor components can be derived by taking a partial derivative of back-propagated wavefield $u_i^b(\mathbf{x}, t)$ with respect to the source coordinates ξ_j

$$\hat{M}_{ij}^{TR}(\xi, t) = \begin{cases} \frac{\partial u_i^b(\mathbf{x}, t)}{\partial \xi_i}, & i = j \\ \frac{\partial u_i^b(\mathbf{x}, t)}{\partial \xi_j} + \frac{\partial u_j^b(\mathbf{x}, t)}{\partial \xi_i}, & i \neq j \end{cases} \quad (5)$$

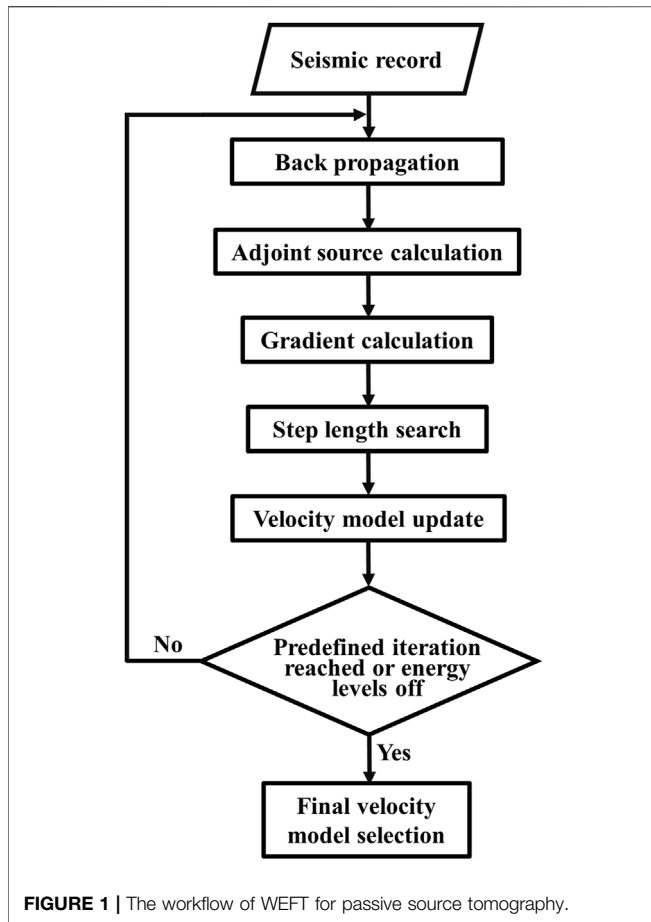


FIGURE 1 | The workflow of WEFT for passive source tomography.

Considering that many well-established seismic location methods, including the ray-based (Waldhauser and Ellsworth, 2000; Zhang and Thurber, 2003; Eisner et al., 2009), migration-based (McMechan, 1982; Artman et al., 2010; Sava, 2011; Nakata and Beroza, 2016; Song and Alkhalifah, 2019; Song et al., 2019b) and full-waveform-based (Kaderli et al., 2015; Wang and Alkhalifah, 2018; Willacy et al., 2019) methods, have been widely employed, we assume that the source locations are provided *a priori* and the influence of location error will be discussed later. To mitigate the effect of the source location error, a spatiotemporal weighting function $w(\mathbf{x}, t)$ is defined for calculating the stacking energy around the source location. Thus, the objective function in Equation 1 can be rewritten as

$$E(v) = -\frac{1}{2} \int_{\tilde{t}_0}^{t_{\max}} \int_{\mathbf{x}} w(\mathbf{x}, t) \left(\left(\frac{\partial u_x^b}{\partial x} \right)^2 + 2 \left(\frac{\partial u_x^b}{\partial z} + \frac{\partial u_z^b}{\partial x} \right)^2 + \left(\frac{\partial u_z^b}{\partial z} \right)^2 \right) dt dx \quad (6)$$

where \mathbf{x} represents spatial coordinates $[x, z]$ in the 2D domain. The spatiotemporal weighting function $w(\mathbf{x}, t)$, which defines a small spatiotemporal cube centered at the source, is given as

$$w(\mathbf{x}, t) = \prod_{\gamma = x, z, t} f \left(\frac{\gamma - \gamma_s}{l_\gamma} \right) T \left(\frac{\gamma - \gamma_s}{l_\gamma} \right) \quad (7)$$

where $\gamma_s \in \{\xi_x, \xi_z, \tilde{t}_0\}$ is the spatiotemporal coordinate of the source, $f \left(\frac{\gamma - \gamma_s}{l_\gamma} \right)$ is a boxcar function whose value is one for $|\frac{\gamma - \gamma_s}{l_\gamma}| \leq 1$ and zero

otherwise, and l_γ defines a small aperture centered at each source coordinate γ_s . $T \left(\frac{\gamma - \gamma_s}{l_\gamma} \right)$ can be a Gaussian taper, a cosine taper, or other types of tapers that make the weighting function smoother. While the temporal aperture (i.e., duration) is determined by the frequency range of the used data, the spatial aperture could be a small value if the initial velocity model and the pre-determined source location are relatively accurate. Otherwise, a larger spatial aperture should be used when the initial velocity model or the pre-determined source location is not accurate.

To update the velocity model, we need to calculate the derivative of $E(v)$ with respect to the velocity $v(\mathbf{X})$ and the adjoint-state method is used (Plessix, 2006). Using the 2D acoustic wave equation, the back-propagation of the wavefield can be expressed as

$$\begin{cases} \frac{\partial v_x^b}{\partial t} + \frac{1}{\rho} \frac{\partial p^b}{\partial x} = f_x \\ \frac{\partial v_z^b}{\partial t} + \frac{1}{\rho} \frac{\partial p^b}{\partial z} = f_z \\ \frac{\partial p^b}{\partial t} + \rho v^2 \left(\frac{\partial v_x^b}{\partial x} + \frac{\partial v_z^b}{\partial z} \right) = 0 \end{cases} \quad (8)$$

where v_x^b and v_z^b are particle velocities and p^b is the pressure. The source f_i is the time-reversed version of observed seismic data d_i ($i \in [x, z]$):

$$f_i(\mathbf{x}, t) = \sum_{r=1}^{nr} \delta(\mathbf{x} - \mathbf{x}_r) d_i(\mathbf{x}_r, t_{\max} - t) \quad (9)$$

According to the Lagrange multiplier method (Hestenes, 1969), we define a new function

$$S(v) = E(v) + \int_{\tilde{t}_0}^{t_{\max}} \int_{\mathbf{x}} \lambda(\mathbf{x}, t) F(v) dx dt \quad (10)$$

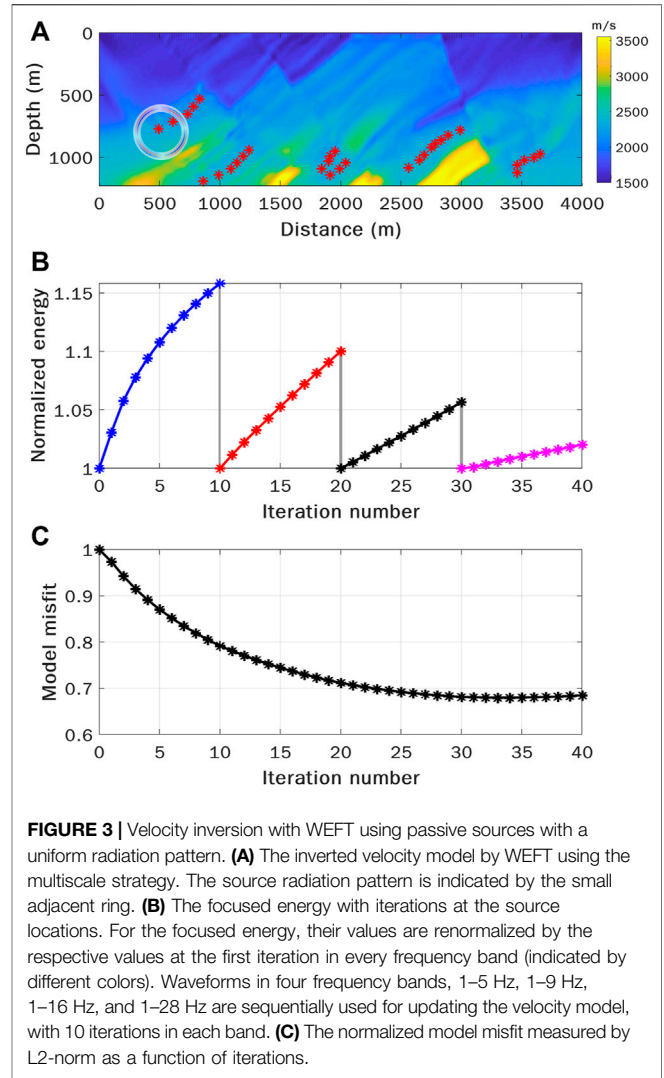
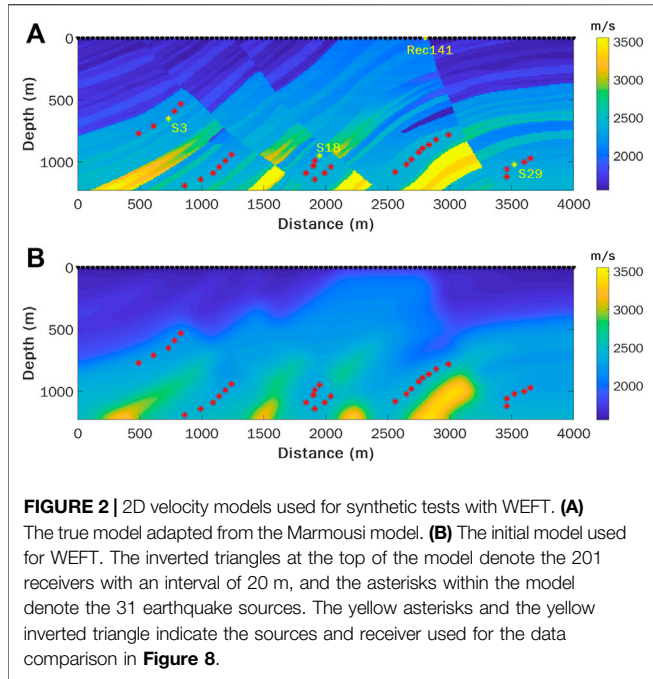
where $\lambda(\mathbf{x}, t) = (\lambda_x, \lambda_z, \lambda_p)^T$ denotes the adjoint-wavefield and Equation 8 can be obtained by setting $F(v) = 0$. Substituting Equations 6, 8 into Equation 10, we obtain

$$\begin{aligned} S(v) = & -\frac{1}{2} \int_{\tilde{t}_0}^{t_{\max}} \int_{\mathbf{x}} w(\mathbf{x}, t) \left(\left(\frac{\partial u_x^b}{\partial x} \right)^2 + 2 \left(\frac{\partial u_x^b}{\partial z} + \frac{\partial u_z^b}{\partial x} \right)^2 + \left(\frac{\partial u_z^b}{\partial z} \right)^2 \right) dt dx + \\ & \int_{\tilde{t}_0}^{t_{\max}} \int_{\mathbf{x}} \lambda_x \left(\frac{\partial v_x^b}{\partial t} + \frac{1}{\rho} \frac{\partial p^b}{\partial x} - f_x \right) dt dx + \int_{\tilde{t}_0}^{t_{\max}} \int_{\mathbf{x}} \lambda_z \left(\frac{\partial v_z^b}{\partial t} + \frac{1}{\rho} \frac{\partial p^b}{\partial z} - f_z \right) dt dx + \\ & \int_{\tilde{t}_0}^{t_{\max}} \int_{\mathbf{x}} \lambda_p \left[\frac{\partial p^b}{\partial t} + \rho v^2 \left(\frac{\partial v_x^b}{\partial x} + \frac{\partial v_z^b}{\partial z} \right) \right] dt dx \end{aligned} \quad (11)$$

where the displacement u_i in the i direction can be expressed as

$$u_i = \int_0^t v_i dt \quad (12)$$

After substituting Equation 12 into Equation 11 and letting the partial derivatives of Equation 11 with respect to v_x^b , v_z^b and p^b equal to zero, we obtain the adjoint-state equation system



$$\begin{cases} \frac{\partial \lambda_x}{\partial t} + \rho v^2 \frac{\partial \lambda_p}{\partial x} = - \int_{\tilde{t}_0}^t w(\mathbf{x}, t) \left(\frac{\partial^2 u_x^b}{\partial x^2} + 2 \frac{\partial^2 u_x^b}{\partial x \partial z} + 2 \frac{\partial^2 u_x^b}{\partial z^2} \right) dt \\ \frac{\partial \lambda_z}{\partial t} + \rho v^2 \frac{\partial \lambda_p}{\partial z} = - \int_{\tilde{t}_0}^t w(\mathbf{x}, t) \left(\frac{\partial^2 u_z^b}{\partial z^2} + 2 \frac{\partial^2 u_z^b}{\partial x \partial z} + 2 \frac{\partial^2 u_z^b}{\partial x^2} \right) dt \\ \frac{\partial \lambda_p}{\partial t} + \frac{1}{\rho} \left(\frac{\partial \lambda_x}{\partial x} + \frac{\partial \lambda_z}{\partial z} \right) = 0 \end{cases} \quad (13)$$

For time-reversal imaging, **Equation 13** can be expressed as

$$\begin{cases} \frac{\partial \lambda_x}{\partial t} + \rho v^2 \frac{\partial \lambda_p}{\partial x} = - \int_{\tilde{t}_0}^t w(\mathbf{x}, t) \left(\frac{\partial \hat{M}_{xx}^{TR}(\mathbf{x}, t)}{\partial x} + 2 \frac{\partial \hat{M}_{xz}^{TR}(\mathbf{x}, t)}{\partial z} \right) dt \\ \frac{\partial \lambda_z}{\partial t} + \rho v^2 \frac{\partial \lambda_p}{\partial z} = - \int_{\tilde{t}_0}^t w(\mathbf{x}, t) \left(\frac{\partial \hat{M}_{zz}^{TR}(\mathbf{x}, t)}{\partial z} + 2 \frac{\partial \hat{M}_{zx}^{TR}(\mathbf{x}, t)}{\partial x} \right) dt \\ \frac{1}{\rho} \left(\frac{\partial \lambda_x}{\partial x} + \frac{\partial \lambda_z}{\partial z} \right) + \frac{\partial \lambda_p}{\partial t} = 0 \end{cases} \quad (14)$$

and the adjoint source of WEFT can be defined as

$$S_i = - \int_{\tilde{t}_0}^t \sum_{j=1}^2 c_{ij} w(\mathbf{x}) \frac{\partial \hat{M}_{ij}^{TR}(\mathbf{x}, t)}{\partial j} dt \quad (15)$$

in which $c_{ij} = 1$ for $i = j$ and $c_{ij} = 2$ otherwise, the adjoint-state equation system can be written as

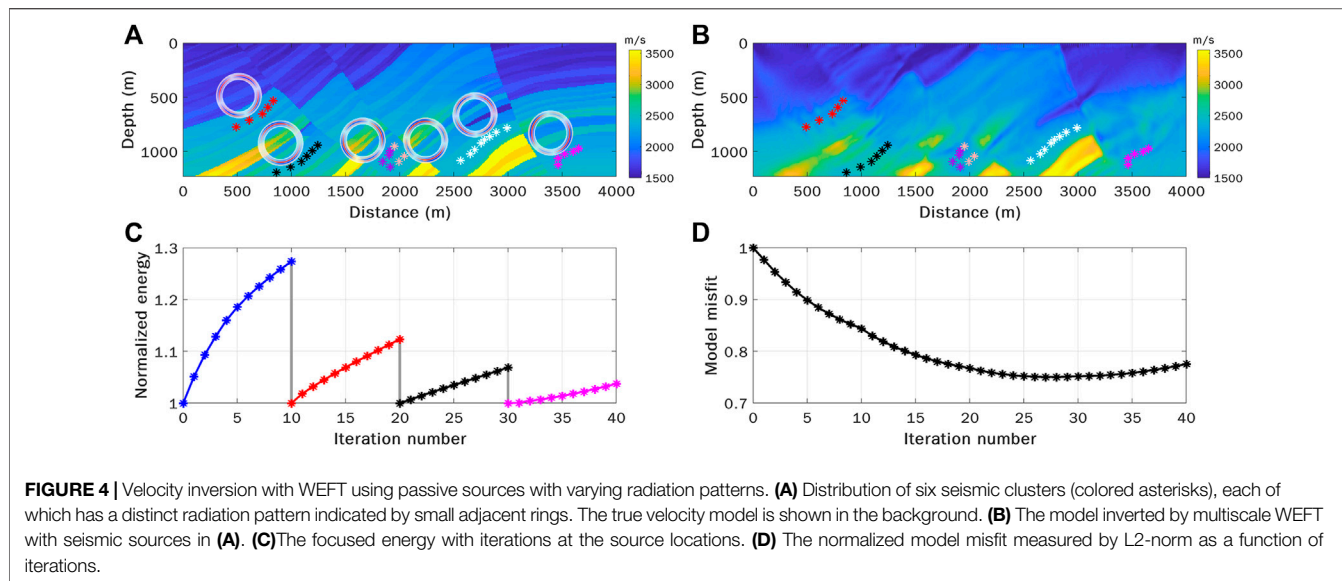
$$\begin{cases} \frac{\partial \lambda_x}{\partial t} + \rho v^2 \frac{\partial \lambda_p}{\partial x} = S_x \\ \frac{\partial \lambda_z}{\partial t} + \rho v^2 \frac{\partial \lambda_p}{\partial z} = S_z \\ \frac{\partial \lambda_p}{\partial t} + \frac{1}{\rho} \left(\frac{\partial \lambda_x}{\partial x} + \frac{\partial \lambda_z}{\partial z} \right) = 0 \end{cases} \quad (16)$$

which is similar to **Equation 8**.

Solving **Equation 11**, the gradient of the objective function can be expressed as

$$\frac{\partial E}{\partial v(\mathbf{x})} = \frac{\partial S(v)}{\partial v(\mathbf{x})} = 2\rho v \int_{\tilde{t}_0}^{t_{max}} \lambda_p \left(\frac{\partial v_x^b}{\partial x} + \frac{\partial v_z^b}{\partial z} \right) dt \quad (17)$$

According to the relationship between the pressure and particle velocity in **Equation 8**, the gradient can be written as



$$\frac{\partial E}{\partial v(\mathbf{x})} = -\frac{2}{v} \int_{t_0}^{t_{\max}} \lambda_p(\mathbf{x}, t; \xi) \frac{\partial p^b(\mathbf{x}, t; \mathbf{x}_r)}{\partial t} dt \quad (18)$$

where $\lambda_p(\mathbf{x}, t; \xi)$ denotes the forward-propagated pressure wavefield excited by the adjoint source of WEFT S_i , and $p^b(\mathbf{x}, t; \mathbf{x}_r)$ denotes the back-propagated pressure wavefield. **Equation 18** means the gradient in WEFT can be calculated by correlating the time derivative of the back-propagated wavefield with forward-propagated wavefield defined by the equation system (**Eq. 16**), which is very similar to FWI (Zhong and Liu, 2019).

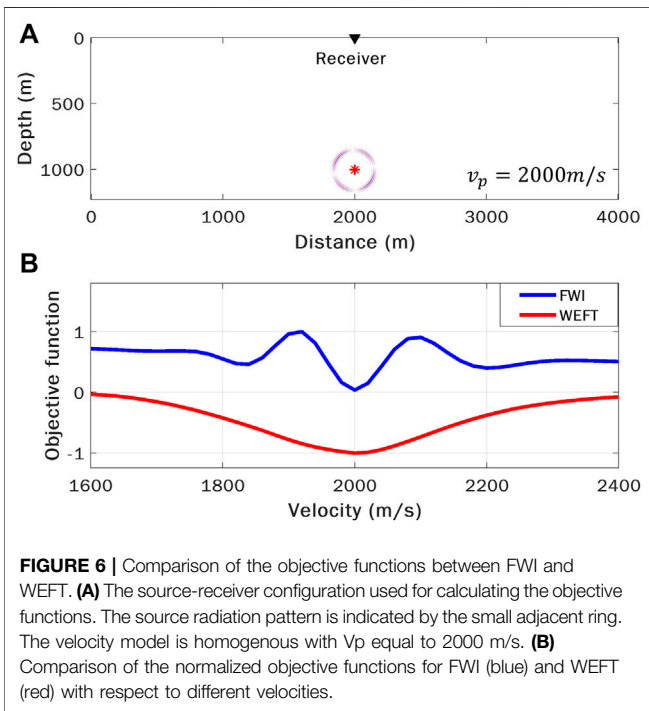
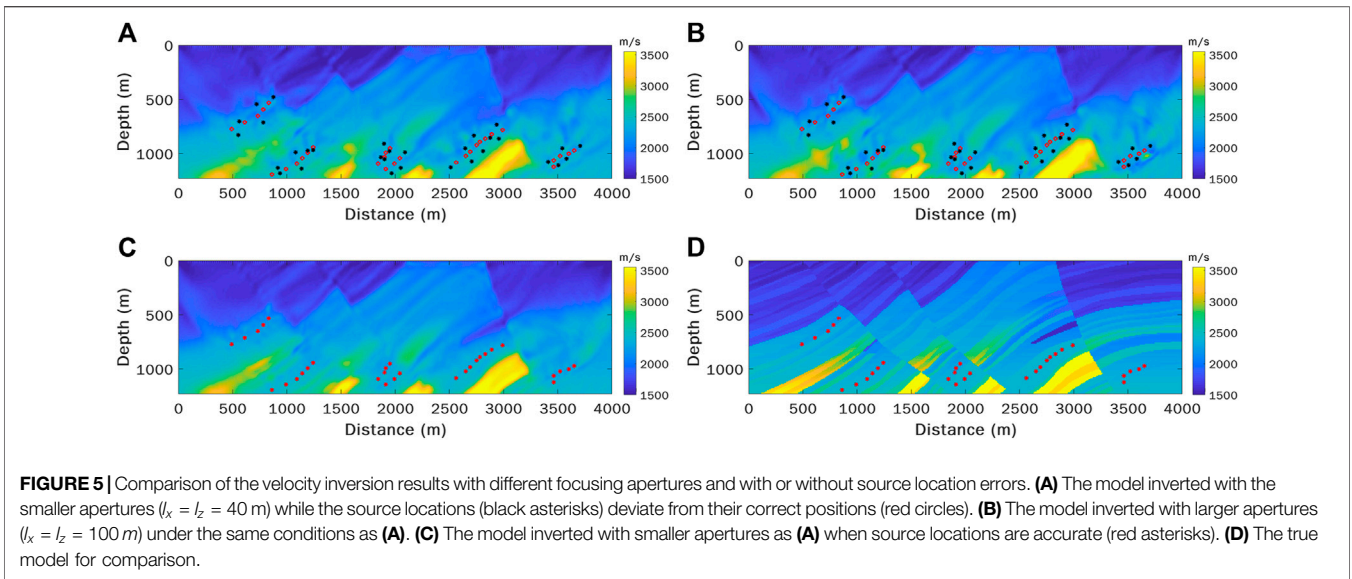
The workflow of WEFT is summarized in **Figure 1**. In each iteration, there are two essential steps: 1) the observed data are first back-propagated and the adjoint source is constructed; 2) the gradient is calculated by correlating the time derivative of back-propagated wavefield with the forward wavefield emanating from the adjoint source according to **Equation 18**. Then the conjugate gradient method (Mora, 1987) is used to update the velocity model iteratively and the backtracking line search method is applied to determine the proper step length. When the predefined number of iterations is reached or the increase in energy levels off, the inversion is terminated. Though there are many similarities in the implementation between WEFT and FWI, some noticeable differences still exist. The major difference is that WEFT back-propagates the recorded seismic data, whereas FWI back-propagates the residual waveforms between the recorded and synthetic data. Moreover, the moment time functions for a source must be provided *a priori* in FWI, whereas the source attributes except for rough source locations are not required for WEFT in advance.

NUMERICAL TESTS

To validate WEFT, we perform a series of synthetic tests using heterogeneous models in 2D. The true velocity model

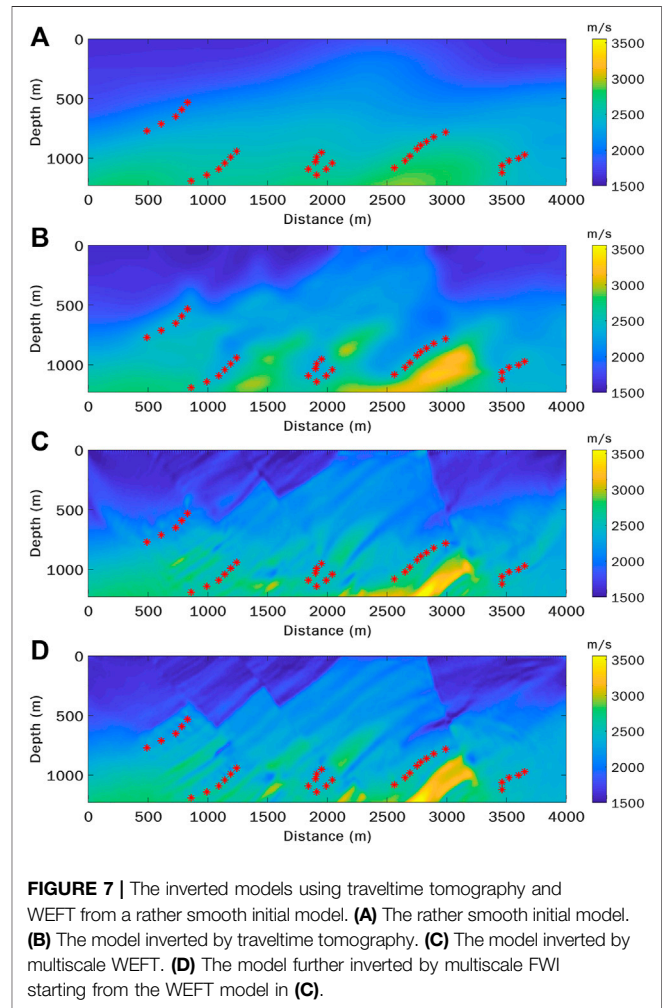
(**Figure 2A**) used for the following numerical experiments is adapted from the widely used Marmousi model (Martin et al., 2002). Both the true and smooth initial velocity models (**Figures 2A,B**) are from Schuster (2017). A Ricker wavelet with central frequency of 15 Hz is chosen as the source time function. The source-receiver configuration consists of 201 receivers on the surface with an interval of 20 m, and 31 passive sources located in the subsurface (**Figure 2**). These sources are distributed into 6 clusters. We should emphasize that the synthetic model used here is for the proof of concept for the proposed WEFT method and may not follow the actual scenarios for earthquake monitoring. However, with more and more dense seismic arrays used for monitoring induced seismicity, the distribution of dense receivers and shallow passive seismic sources are actually expected, such as the dense geophones used for monitoring shale gas hydraulic fracturing (Eisner et al., 2010; Staněk and Eisner, 2013; Anikiev et al., 2014).

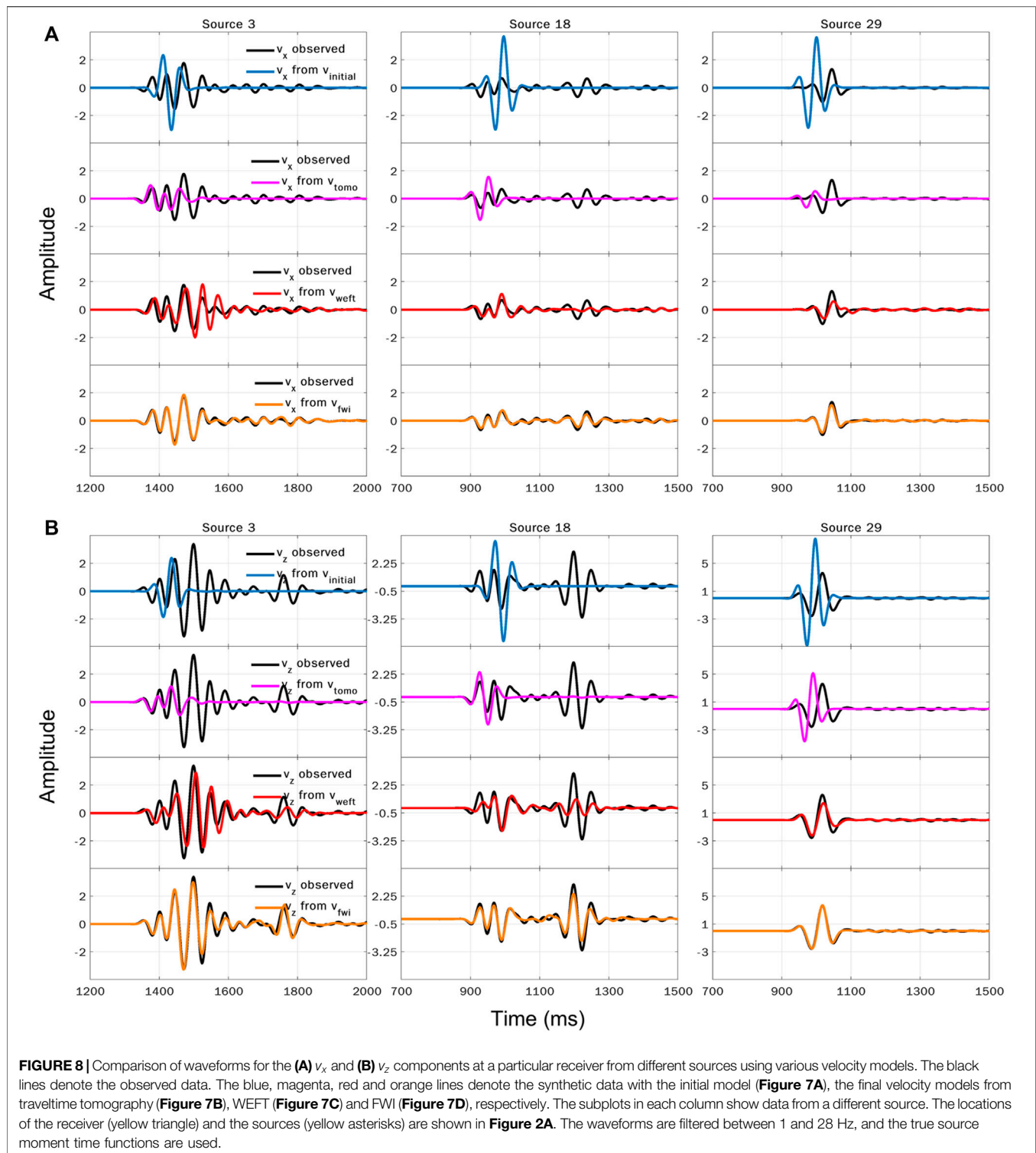
Following the approach now commonly used in FWI, which sequentially utilizes observed data with increasing frequencies (Bunks et al., 1995), a multiscale strategy is also adopted in WEFT. After a predefined number of iterations is reached for a certain frequency band, the final velocity model is used as the initial model for the next frequency band. Since the source location used in this case is accurate, we choose a small spatial aperture $l_x = l_z = 40$ m, and the temporal aperture is larger than the half-width of the source wavelet. To improve the resolution of the inverted model, the spatial aperture $l_{x,z}$ in **Eq. 7** for evaluating the focused energy is gradually decreased with increasing frequencies. We first test the WEFT using passive seismic sources with a uniform radiation pattern (indicated by the small adjacent ring in **Figure 3A**). Four frequency bands of 1–5 Hz, 1–9 Hz, 1–16 Hz, and 1–28 Hz are adopted. It can be seen that the inverted model (**Figure 3A**) is hardly affected by the source radiation pattern although the source moment time function is not provided for the inversion. The focused energy (**Figure 3B**) increases with iterations in each frequency band and



its growth levels off gradually. Meanwhile, the model misfit measured by the L2-norm also decreases with iterations, as shown in **Figure 3C**.

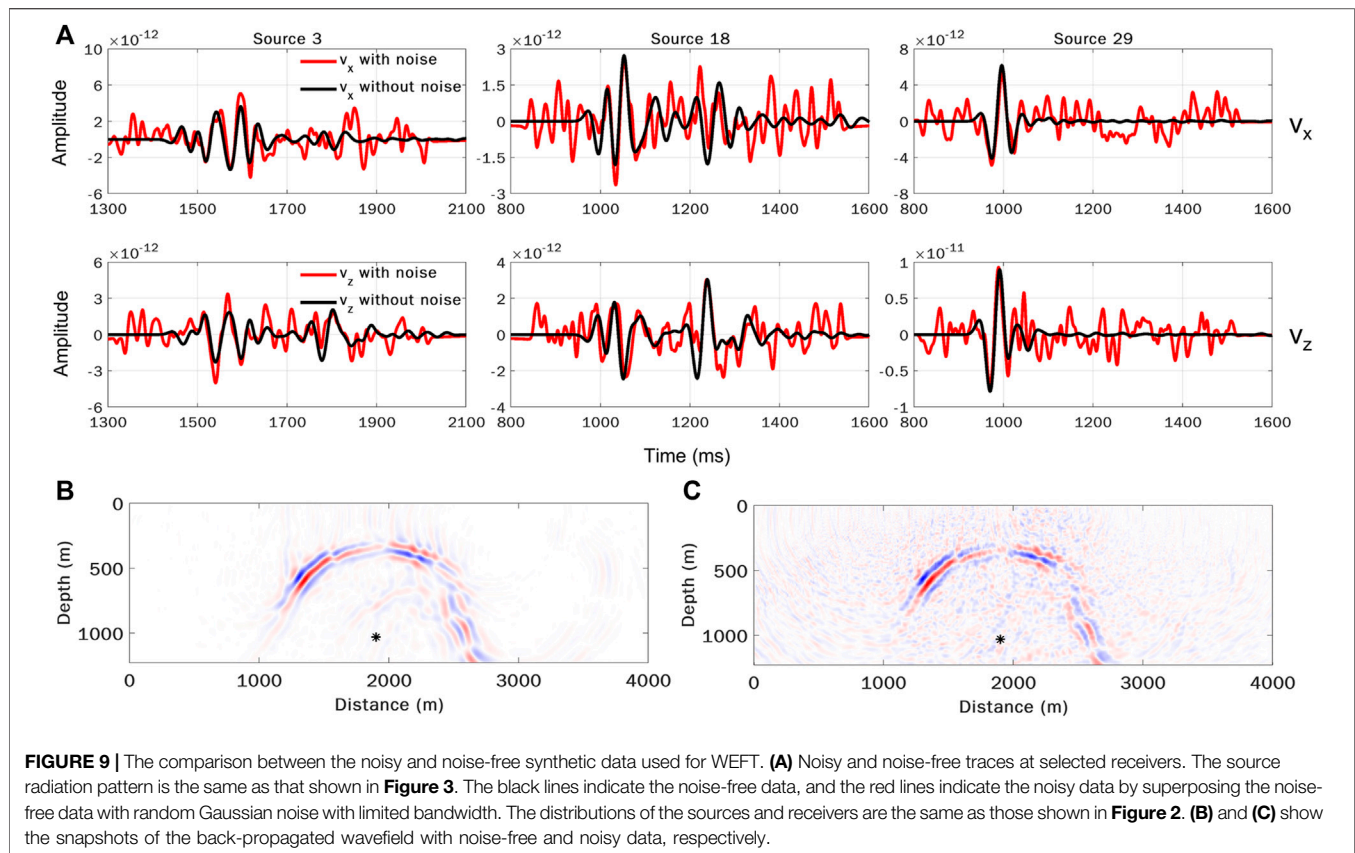
We further test a more complicated scenario where six seismic clusters having different types of source moment tensors (**Figure 4A**). The spatiotemporal aperture used here is the same as in the previous case. The model inverted by the multiscale WEFT is shown in **Figure 4B**. Though the varying





radiation patterns from different clusters pose a considerable challenge for waveform inversion, WEFT still inverts for the heterogeneous Marmousi model accurately. Compared to the true model, there are some minor artifacts in the inverted model, which are probably caused by the varying radiation patterns that can result in complicated directional illuminations in resolving

the model. Although the stacking energy (Figure 4C) increases with iteration in each frequency band as expected, the model misfit (Figure 4D) undesirably also increases slightly in the last frequency band, which suggests the inversion was trapped in a local minimum for high-frequency data. Nevertheless, this example demonstrates that WEFT can be applied directly to



surface seismic monitoring datasets in which seismic sources occur on different faults are with varying orientations and slipping angles.

DISCUSSIONS

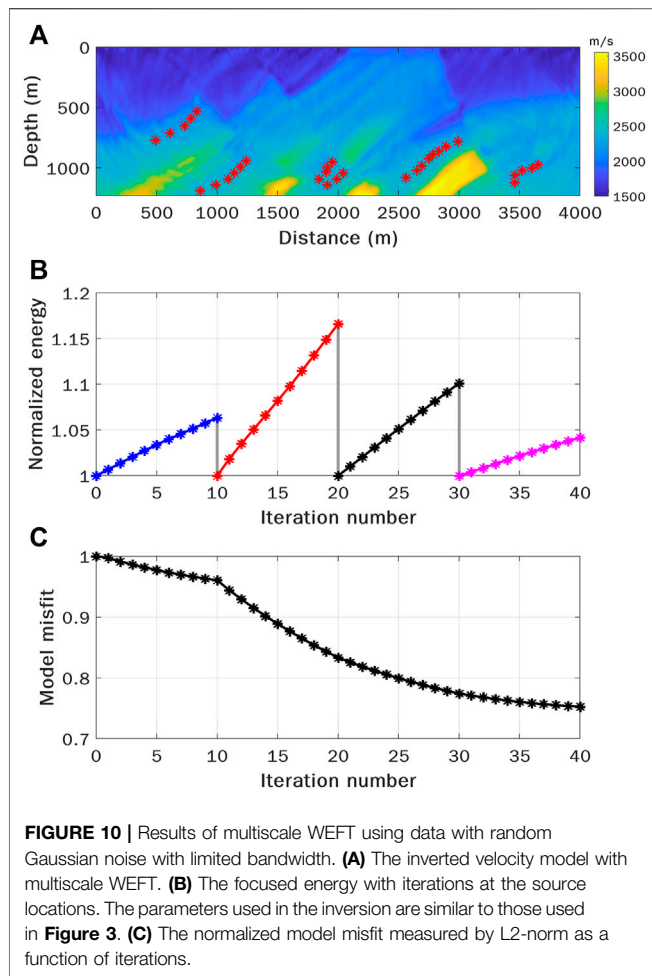
Influence of Uncertainty in Source Location

In WEFT, the source location is used to determine the spatial volume for evaluating the focused energy (**Equation 7**), and for the adjoint source injection when calculating the adjoint wavefield (λ_p in **Equation 15**). As discussed earlier, in WEFT it is assumed that the source location and origin time are predetermined from other methods, e.g., the NonLinLoc method (Lomax et al., 2000), the double-difference location method based on traveltimes (Waldhauser and Ellsworth, 2000; Zhang and Thurber, 2003), or the recently developed location methods based on machine learning (Kriegerowski et al., 2019; Zhang et al., 2020; Wang and Alkhalifah, 2021). Thus, the source location may deviate from its true position owing to an inaccurate velocity model (Thurber, 1992) and arrival times. In WEFT, a way to mitigate the influence of inaccurate source locations is to expand the spatial aperture for evaluating the focused energy (determined by l_x and l_z in **Equation 7**). That is, the spatial aperture should be designed based on the source location uncertainty so that the true location is contained in the volume for evaluating the focused energy. To some extent,

however, this strategy may also compromise the accuracy and resolution of the inverted velocity model, since the back-propagated wavefields using a slightly incorrect model may still focus well within an enlarged volume. When the source locations are known accurately, the inverted model using a smaller spatial aperture with $l_x = l_z = 40$ m is shown in **Figure 5C**, and the model misfit is reduced by about 30%. However, when the source locations are not accurate, the result using the same spatial apertures shows a slightly distorted inclined high-velocity layer at the bottom of the model ($x \approx 3000$ m, $z \approx 1000$ m) and a blurred inclined thin layer with low velocity ($x \approx 3000$ m, $z \approx 600$ m) (**Figure 5A**). The model misfit in this case is only reduced by 10%. If we enlarge the apertures to $l_x = l_z = 100$ m, not only the model misfit is reduced by about 18% of the original, but also the distortion is suppressed and the low-velocity thin layer is better recovered (**Figure 5B**). By comparing models in **Figure 5A,B,C**, we notice that some artifacts around the sources are introduced with inaccurate source locations.

Comparison With Full Waveform Inversion and Seismic Travel Time Tomography

Since WEFT evaluates the magnitudes of the back-propagated energy focused around the hypocenters instead of matching the wiggles between the observed and synthetic waveforms at the receivers, the proposed method has less nonlinearity and is more



robust since there is less cycle-skipping issues as commonly seen in conventional FWI. **Figure 6B** shows a comparison of objective functions of FWI and WEFT for a simple source-receiver configuration (**Figure 6A**), where the passive source is located at 1,000 m in depth and a single receiver is on the surface. It is obvious that the objective function of FWI has multiple local minima compared to that of WEFT, which has a more convex behavior globally and has only a single global minimum for this scenario.

The lower nonlinearity of WEFT can also facilitate velocity inversion from a poor initial velocity model. In **Figure 7**, we further compare the inversion results between WEFT and conventional traveltime tomography using an even smoother initial velocity model (**Figure 7A**). Compared to the true model, many small heterogeneities and contrasts are recovered in the inverted model by WEFT (**Figure 7C**), while only the tilted high-velocity bodies at the bottom of the model are distorted. In comparison, the inverted model by traveltime tomography (**Figure 7B**) appears much smoother and lack fine details. Starting from the final inverted model from WEFT, we perform FWI to further update the velocity (**Figure 7D**), and even more details are added to the model. It should be stressed again that WEFT does not require source moment time functions

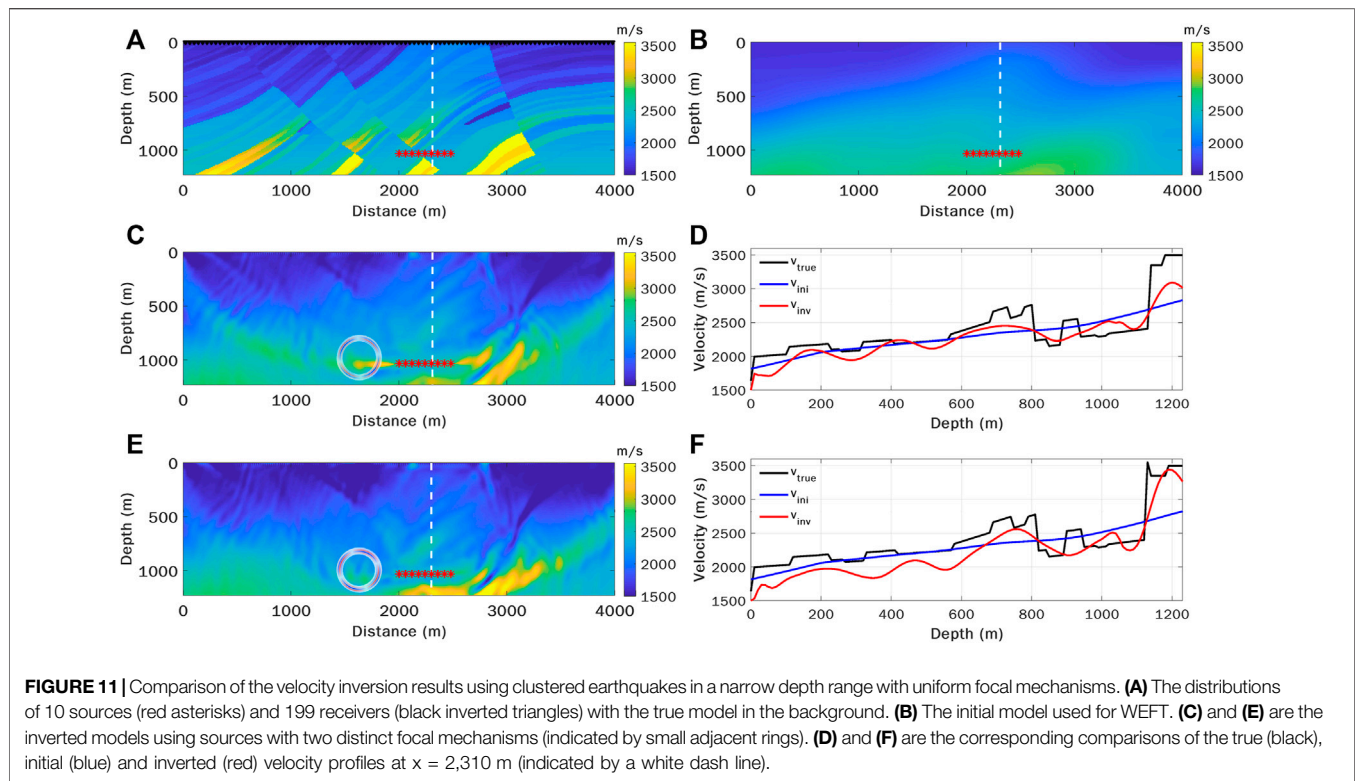
in the inversion, while FWI does. Using the final velocity models inverted by WEFT and traveltime tomography shown in **Figure 7**, we generate synthetic waveforms and compare the v_x and v_z components (**Figure 8**). Significant time delays can be found between the “observed” data from the true model (black lines) and the ‘synthetic’ data generated based on the initial model (blue lines). Although the model inverted by traveltime tomography considerably mitigates the time delays between the observed and synthetic data, wiggles in the two datasets still differ markedly. In comparison, the waveform matching between the synthetic and observed data improves considerably using the velocity model derived by WEFT, with many later-arrived wiggles successfully modeled. When using the model inverted by FWI starting from the final model of WEFT, the synthetic and observed waveforms are almost the same. This nice agreement in waveforms indicates that though the objective function of WEFT only considers the energy focusing at the sources directly, the waveform matching at the receivers is nevertheless satisfactory owing to a correctly updated model.

Influence of Noise

We further test the stability and accuracy of WEFT with noisy observed data (**Figure 9A**). In this experiment, the synthetic data are contaminated by random Gaussian noise, which is not coherent among receivers, and the SNR is about 0.3. For the noisy data, it is difficult to obtain a relatively accurate velocity model by conventional FWI without sophisticated data preprocessing. However, it is still possible to apply WEFT with the noisy data. This is because although the seismic signals are initially buried in the noise, the coherent signals can be gradually enhanced against the inherent noise with back-propagation. In other words, wavefield back-propagation specifically focuses the energy of the microseismic event and thus suppresses incoherent noise, which can be seen in the snapshots of the back-propagated wavefields at a certain time with noise-free and noisy data (**Figures 9B,C**, respectively). Compared with the inverted model from the noise-free data (**Figure 3**), the inverted model with the noisy data is similar (**Figure 10A**), and the model misfit (**Figure 10C**) still shows a considerable reduction. This test demonstrates that WEFT is rather resilient to incoherent noise, which can be a considerable advantage over FWI.

Influence of Source Distribution

Considering that the distribution of sources and the source mechanisms may have a noticeable influence on the inverted model, we further perform a challenging test where 10 earthquakes with a uniform radiation pattern are distributed within a narrow depth range of 60 m, as shown in **Figure 11A**. Starting from the initial model shown in **Figure 11B**, two distinct source mechanisms are used for comparison. The inverted models using sources with different radiation patterns (indicated by the small adjacent ring) are shown in **Figures 11C,E**, respectively. The comparison of the velocity profiles at the position $x = 2,310$ m is shown in **Figures 11D,F**, respectively. We found that, as expected, most of the effective update is within the central part of the model above the earthquake sources due to the limited source illumination.



Besides, different source mechanisms, which result in varying illumination patterns, inevitably have an impact on the inverted models. Due to the poor source distribution, the recovered models are not as good as those shown before. However, both inverted models are updated successfully compared to the initial one, especially the model shown in **Figures 11C,D**.

CONCLUSION

We propose a new seismic tomography method called Waveform Energy Focusing Tomography for passive seismic sources. Compared to FWI, WEFT inverts for the velocity model by maximizing the energy of the moment time functions from back-propagated wavefields around the sources, instead of matching synthetic and observed waveforms at the receivers. As a result, WEFT has lower nonlinearity in the inversion and can avoid the cycle skipping issue in FWI. More importantly, except for the source locations and origin times, WEFT does not require other source attributes including source time functions and focal mechanisms. This means that more earthquakes with smaller magnitudes and unknown source mechanisms can also be used by WEFT.

We have shown the effectiveness and advantages of WEFT through several 2D synthetic tests based on the Marmousi model. WEFT can still perform well on different challenging cases when passive seismic sources have different radiation patterns, when the initial velocity model is rather smooth, and when waveforms are very noisy. Nevertheless, the quality of inverted models can still be affected by uneven illumination due to distributions and mechanisms of sources. Although waveform matching at the

receivers is not directly considered in the objective function of WEFT, the synthetic tests show that the waveform matching using the inverted model by WEFT is still satisfactory, much better than the velocity model inverted by traveltime tomography using arrival times. It should be noted that WEFT yields velocity models with slightly lower resolution compared to FWI. Therefore, WEFT can act as an intermediate step between seismic traveltime tomography and FWI by providing a more accurate and reliable starting velocity model for the latter.

In this study, for simplicity we validate WEFT with passive seismic sources under the 2D acoustic assumption. This method can also be extended to 3D for real applications such as dense-array monitoring of local seismicity from fault zones or hydraulic fracturing when the receivers are not distributed along a straight line or the passive sources have an areal distribution, which will be shown in a future study.

DATA AVAILABILITY STATEMENT

The raw data supporting the conclusions of this article will be made available by the authors, without undue reservation.

AUTHOR CONTRIBUTIONS

YH, JL, and HZ all contributed to the study. YH performed the numerical tests and wrote the first draft of the manuscript. All authors contributed to the revision and approved the submitted version.

FUNDING

This research is supported by the National Natural Science Foundation of China under grants 41961134001 and 41874048, and supported by the National Key Research and Development Projects 2021YFC3000602 and 2018YFC1504102.

REFERENCES

- Adamczyk, A., Malinowski, M., and Górszczyk, A. (2015). Full-waveform Inversion of Conventional Vibroseis Data Recorded along a Regional Profile from Southeast Poland. *Geophys. J. Int.* 203, 351–365. doi:10.1093/gji/ggv305
- Alkhalifah, T. (2014). *Full Waveform Inversion in an Anisotropic World: Where Are the Parameters Hiding*. European Association of Geoscientists and Engineers (EAGE).
- Alkhalifah, T., and Song, C. (2019). An Efficient Wavefield Inversion: Using a Modified Source Function in the Wave Equation. *Geophysics* 84, R909–R922. doi:10.1190/geo2018-0759.1
- Anikiev, D., Valenta, J., Staněk, F., and Eisner, L. (2014). Joint Location and Source Mechanism Inversion of Microseismic Events: Benchmarking on Seismicity Induced by Hydraulic Fracturing. *Geophys. J. Int.* 198 (1), 249–258. doi:10.1093/gji/ggu126
- Artman, B., Podladtchikov, I., and Witten, B. (2010). Source Location Using Time-Reverse Imaging. *Geophys. Prospect.* 58, 861–873. doi:10.1111/j.1365-2478.2010.00911.x
- Bazargani, F., and Snieder, R. (2016). Optimal Source Imaging in Elastic Media. *Geophys. J. Int.* 204, 1134–1147. doi:10.1093/gji/ggv494
- Biondi, B., and Almomin, A. (2014). Simultaneous Inversion of Full Data Bandwidth by Tomographic Full-Waveform Inversion. *Geophysics* 79, WA129–WA140. doi:10.1190/geo2013-0340.1
- Bleibinhaus, F., Hole, J. A., Ryberg, T., and Fuis, G. S. (2007). Structure of the California Coast Ranges and San Andreas Fault at SAFOD from Seismic Waveform Inversion and Reflection Imaging. *J. Geophys. Res. Solid Earth* 112, 4611. doi:10.1029/2006jb004611
- Bording, R. P., Gersztenkorn, A., Lines, L. R., Scales, J. A., and Treitel, S. (1987). Applications of Seismic Travel-Time Tomography. *Geophys. J. Int.* 90, 285–303. doi:10.1111/j.1365-246x.1987.tb00728.x
- Bozdağ, E., Peter, D., Lefebvre, M., Komatitsch, D., Tromp, J., Hill, J., et al. (2016). Global Adjoint Tomography: First-Generation Model. *Geophys. J. Int.* 207, 1739–1766. doi:10.1093/gji/ggw356
- Bozdağ, E., Trampert, J., and Tromp, J. (2011). Misfit Functions for Full Waveform Inversion Based on Instantaneous Phase and Envelope Measurements. *Geophys. J. Int.* 185, 845–870. doi:10.1111/j.1365-246X.2011.04970.x
- Brenders, A. J., and Pratt, R. G. (2007). Full Waveform Tomography for Lithospheric Imaging: Results from a Blind Test in a Realistic Crustal Model. *Geophys. J. Int.* 168, 133–151. doi:10.1111/j.1365-246x.2006.03156.x
- Bunks, C., Saleck, F. M., Zaleski, S., and Chavent, G. (1995). Multiscale Seismic Waveform Inversion. *Geophysics* 60, 1457–1473. doi:10.1190/1.1443880
- Chambers, K., Dando, B. D. E., Jones, G. A., Velasco, R., and Wilson, S. A. (2014). Moment Tensor Migration Imaging. *Geophys. Prospect.* 62, 879–896. doi:10.1111/1365-2478.12108
- Cheong, S., Pyun, S., and Shin, C. (2006). Two Efficient Steepest-Descent Algorithms for Source Signature-free Waveform Inversion: Synthetic Examples. *J. Seismic Explor.* 14, 335.
- Choi, Y., and Alkhalifah, T. (2011). Source-independent Time-Domain Waveform Inversion Using Convolved Wavefields: Application to the Encoded Multisource Waveform Inversion. *Geophysics* 76, R125–R134. doi:10.1190/geo2010-0210.1
- Choi, Y., and Alkhalifah, T. (2015). Unwrapped Phase Inversion with an Exponential Damping. *Geophysics* 80, R251–R264. doi:10.1190/geo2014-0498.1
- Choi, Y., Shin, C., Min, D.-J., and Ha, T. (2005). Efficient Calculation of the Steepest Descent Direction for Source-independent Seismic Waveform Inversion: An Amplitude Approach. *J. Comput. Phys.* 208, 455–468. doi:10.1016/j.jcp.2004.09.019
- Eisner, L., Duncan, P. M., Heigl, W. M., and Keller, W. R. (2009). Uncertainties in Passive Seismic Monitoring. *Lead. Edge* 28, 648–655. doi:10.1190/1.3148403
- Eisner, L., Williams-Stroud, S., Hill, A., Duncan, P., and Thornton, M. (2010). Beyond the Dots in the Box: Microseismicity-Constrained Fracture Models for Reservoir Simulation. *Lead. Edge* 29 (3), 326–333. doi:10.1190/1.3353730
- Engquist, B., and Froese, B. D. (2013). Application of the Wasserstein Metric to Seismic Signals. arXiv preprint arXiv:1311.4581.
- Eyre, T. S., and van der Baan, M. (2015). Overview of Moment-Tensor Inversion of Microseismic Events. *Lead. Edge* 34, 882–888. doi:10.1190/tle34080882.1
- Fichtner, A., Kennett, B. L. N., Igel, H., and Bunge, H.-P. (2009). Full Seismic Waveform Tomography for Upper-Mantle Structure in the Australasian Region Using Adjoint Methods. *Geophys. J. Int.* 179, 1703–1725. doi:10.1111/j.1365-246x.2009.04368.x
- Fichtner, A., Trampert, J., Cupillard, P., Saygin, E., Taymaz, T., Capdeville, Y., et al. (2013). Multiscale Full Waveform Inversion. *Geophys. J. Int.* 194, 534–556. doi:10.1093/gji/ggt118
- Fink, M. (1997). Time Reversed Acoustics. *Phys. today* 50, 34–40. doi:10.1063/1.881692
- Gharti, H. N., Oye, V., Kühn, D., and Zhao, P. (2011). “Simultaneous Microearthquake Location and Moment-Tensor Estimation Using Time-Reversal Imaging,” in 81st Annual International Meeting, SEG Technical Program Expanded Abstracts 2011, San Antonio, 1632–1637.
- Hara, S., Fukahata, Y., and Iio, Y. (2019). P Wave First-Motion Polarity Determination of Waveform Data in Western Japan Using Deep Learning. *Earth Planets Space* 71, 1–11. doi:10.1186/s40623-019-1111-x
- Hardebeck, J. L., and Shearer, P. M. (2002). A New Method for Determining First-Motion Focal Mechanisms. *Bull. Seismol. Soc. Am.* 92, 2264–2276. doi:10.1785/0120010200
- Hardebeck, J. L., and Shearer, P. M. (2003). Using S/P Amplitude Ratios to Constrain the Focal Mechanisms of Small Earthquakes. *Bull. Seismol. Soc. Am.* 93, 2434–2444. doi:10.1785/0120020236
- Hestenes, M. R. (1969). Multiplier and Gradient Methods. *J. Optim. Theory Appl.* 4, 303–320. doi:10.1007/bf00927673
- Huang, G., Nammour, R., and Symes, W. (2017). Full-waveform Inversion via Source-Receiver Extension. *Geophysics* 82, R153–R171. doi:10.1190/geo2016-0301.1
- Jin, S., and Plessix, R.-É. (2013). “Stack-based Full Wavefield Velocity Tomography,” in 83rd Annual International Meeting, SEG Technical Program Expanded Abstracts 2013, Houston, 1095–1099. doi:10.1190/segam2013-1027.1
- Julian, B. R., Miller, A. D., and Foulger, G. R. (1998). Non-double-couple Earthquakes 1. Theory. *Rev. Geophys.* 36, 525–549. doi:10.1029/98rg00716
- Kaderli, J., McChesney, M. D., and Minkoff, S. E. (2015). “Microseismic Event Estimation in Noisy Data via Full Waveform Inversion,” in 85th Annual International Meeting, SEG Technical Program Expanded Abstracts 2015, New Orleans, 1159–1164. doi:10.1190/segam2015-5867154.1
- Kawakatsu, H., and Montagner, J.-P. (2008). Time-reversal Seismic-Source Imaging and Moment-Tensor Inversion. *Geophys. J. Int.* 175, 686–688. doi:10.1111/j.1365-246x.2008.03926.x
- Kim, Y., Liu, Q., and Tromp, J. (2011). Adjoint Centroid-Moment Tensor Inversions. *Geophys. J. Int.* 186, 264–278. doi:10.1111/j.1365-246x.2011.05027.x
- Kissling, E., Kradolfer, U., and Maurer, H. (1995). *Program VELEST User's Guide-Short Introduction*. ETH Zurich: Institute of Geophysics.
- Kriegerowski, M., Petersen, G. M., Vasyura-Bathke, H., and Ohrnberger, M. (2019). A Deep Convolutional Neural Network for Localization of Clustered Earthquakes Based on Multistation Full Waveforms. *Seismol. Res. Lett.* 90, 510–516. doi:10.1785/0220180320
- Kuang, W., Yuan, C., and Zhang, J. (2021). Real-time Determination of Earthquake Focal Mechanism via Deep Learning. *Nat. Commun.* 12, 1–8. doi:10.1038/s41467-021-21670-x

ACKNOWLEDGMENTS

The authors would like to thank Haipeng Li for his many helpful discussions. We also thank two reviewers and editor Tariq Alkhalifah for their very helpful comments in improving our manuscript.

- Lanz, E., Maurer, H., and Green, A. G. (1998). Refraction Tomography over a Buried Waste Disposal Site. *Geophysics* 63, 1414–1433. doi:10.1190/1.1444443
- Larmat, C., Montagner, J. P., Fink, M., Capdeville, Y., Tourin, A., and Clévéde, E. (2006). Time-reversal Imaging of Seismic Sources and Application to the Great Sumatra Earthquake. *Geophys. Res. Lett.* 33, 26336. doi:10.1029/2006GL026336
- Lee, K. H., and Kim, H. J. (2003). Source-independent Full-waveform Inversion of Seismic Data. *Geophysics* 68, 2010–2015. doi:10.1190/1.1635054
- Lellouch, A., and Landa, E. (2018). Seismic Velocity Estimation Using Time-Reversal Focusing. *Geophysics* 83 (4), U43–U50. doi:10.1190/geo2017-0569.1
- Li, J., Zhang, H., Sadi Kuleli, H., and Nafi Toksoz, M. (2011). Focal Mechanism Determination Using High-Frequency Waveform Matching and its Application to Small Magnitude Induced Earthquakes. *Geophys. J. Int.* 184, 1261–1274. doi:10.1111/j.1365-246x.2010.04903.x
- Li, Y., and Alkhalifah, T. (2021). Extended Full Waveform Inversion with Matching Filter. *Geophys. Prospect.* 69 (7), 1441–1454. doi:10.1111/1365-2478.13121
- Lomax, A., Virieux, J., Volant, P., and Berge-Thierry, C. (2000). “Probabilistic Earthquake Location in 3D and Layered Models,” in *Advances in Seismic Event Location*. Editors C. H. Thurber and N. Rabinowitz (Amsterdam: Kluwer), 101–134. doi:10.1007/978-94-015-9536-0_5
- Luo, J., and Wu, R.-S. (2015). Seismic Envelope Inversion: Reduction of Local Minima and Noise Resistance. *Geophys. Prospect.* 63, 597–614. doi:10.1111/1365-2478.12208
- Luo, S., and Sava, P. (2011). “A Deconvolution-Based Objective Function for Wave-Equation Inversion,” in 81st Annual International Meeting, SEG Technical Program Expanded Abstracts 2011, San Antonio, 2788–2792. doi:10.1190/1.3627773
- Luo, Y., and Schuster, G. T. (1991). Wave-equation Traveltime Inversion. *Geophysics* 56, 645–653. doi:10.1190/1.1443081
- Lyu, B., and Nakata, N. (2020). Iterative Passive-Source Location Estimation and Velocity Inversion Using Geometric-Mean Reverse-Time Migration and Full-Waveform Inversion. *Geophys. J. Int.* 223, 1935–1947. doi:10.1093/gji/ggaa428
- Martin, G. S., Marfurt, K. J., and Larsen, S. (2002). “Marmousi-2: An Updated Model for the Investigation of AVO in Structurally Complex Areas,” in SEG International Exposition and 72nd Annual International Meeting, SEG Technical Program Expanded Abstracts 2002, Salt Lake City, UT.
- McMechan, G. A. (1982). Determination of Source Parameters by Wavefield Extrapolation. *Geophys. J. Int.* 71, 613–628. doi:10.1111/j.1365-246x.1982.tb02788.x
- Métivier, L., Brossier, R., Merigot, Q., Oudet, É., and Virieux, J. (2016). An Optimal Transport Approach for Seismic Tomography: Application to 3D Full Waveform Inversion. *Inverse Probl.* 32, 115008. doi:10.1088/0266-5611/32/11/115008
- Mora, P. (1987). Nonlinear Two-dimensional Elastic Inversion of Multioffset Seismic Data. *Geophysics* 52, 1211–1228. doi:10.1190/1.1442384
- Nakata, N., and Beroza, G. C. (2016). Reverse Time Migration for Microseismic Sources Using the Geometric Mean as an Imaging Condition. *Geophysics* 81, KS51–KS60. doi:10.1190/geo2015-0278.1
- Oh, J.-W., and Alkhalifah, T. (2018). Full Waveform Inversion Using Envelope-Based Global Correlation Norm. *Geophys. J. Int.* 213, 815–823. doi:10.1093/gji/ggy031
- Operto, S., Miniussi, A., Brossier, R., Combe, L., Métivier, L., Monteiller, V., et al. (2015). Efficient 3-D Frequency-Domain Mono-Parameter Full-Waveform Inversion of Ocean-Bottom Cable Data: Application to Valhall in the Visco-Acoustic Vertical Transverse Isotropic Approximation. *Geophys. J. Int.* 202, 1362–1391. doi:10.1093/gji/ggv226
- Oren, C., and Shragge, J. (2022). Passive-seismic Image-Domain Elastic Wavefield Tomography. *Geophys. J. Int.* 228 (3), 1512–1529. doi:10.1093/gji/ggab415
- Oren, C., and Shragge, J. (2021). PS Energy Imaging Condition for Microseismic Data - Part 1: Theory and Applications in 3D Isotropic Media. *Geophysics* 86 (2), KS37–KS48. doi:10.1190/geo2020-0476.1
- Plessix, R.-E. (2006). A Review of the Adjoint-State Method for Computing the Gradient of a Functional with Geophysical Applications. *Geophys. J. Int.* 167, 495–503. doi:10.1111/j.1365-246x.2006.02978.x
- Pratt, R. G. (1999). Seismic Waveform Inversion in the Frequency Domain, Part 1: Theory and Verification in a Physical Scale Model. *Geophysics* 64, 888–901. doi:10.1190/1.1444597
- Pratt, R. G., and Worthington, M. H. (1990). Inverse Theory Applied to Multi-Source Cross-Hole Tomography. Part 1: Acoustic Wave-Equation Method. *Geophys. Prospect* 38, 287–310. doi:10.1111/j.1365-2478.1990.tb01846.x
- Rau, R.-J., Wu, F. T., and Shin, T.-C. (1996). Regional Network Focal Mechanism Determination Using 3D Velocity Model and SH/P Amplitude Ratio. *Bull. Seismol. Soc. Am.* 86, 1270–1283.
- Ravaut, C., Operto, S., Improta, L., Virieux, J., Herrero, A., and Dell’Aversana, P. (2004). Multiscale Imaging of Complex Structures from Multifold Wide-Aperture Seismic Data by Frequency-Domain Full-Waveform Tomography: Application to a Thrust Belt. *Geophys. J. Int.* 159, 1032–1056. doi:10.1111/j.1365-246x.2004.02442.x
- Rawlinson, N., and Sambridge, M. (2003). Seismic Traveltime Tomography of the Crust and Lithosphere. *Adv. Geophys.* 46, 81–198. doi:10.1016/s0065-2687(03)46002-0
- Rocha, D., Sava, P., Shragge, J., and Witten, B. (2019). 3D Passive Wavefield Imaging Using the Energy Norm. *Geophysics* 84 (2), KS13–KS27. doi:10.1190/geo2018-0251.1
- Ross, Z. E., Meier, M. A., and Hauksson, E. (2018). P Wave Arrival Picking and First-Motion Polarity Determination with Deep Learning. *J. Geophys. Res. Solid Earth* 123, 5120–5129. doi:10.1029/2017jb015251
- Sava, P. (2011). Micro-earthquake Monitoring with Sparsely Sampled Data. *J. Pet. Explor. Prod. Technol.* 1, 43–49. doi:10.1007/s13202-011-0005-7
- Schuster, G. T. (2017). *Seismic Inversion*. Society of Exploration Geophysicists (SEG). Available at: <https://csim.kaust.edu.sa/files/ErSE328.2013/LAB/Chapter.FW1a/index.html>.
- Shin, C., and Cha, Y. H. (2009). Waveform Inversion in the Laplace-Fourier Domain. *Geophys. J. Int.* 177, 1067–1079. doi:10.1111/j.1365-246x.2009.04102.x
- Shin, C., and Cha, Y. H. (2008). Waveform Inversion in the Laplace Domain. *Geophys. J. Int.* 173, 922–931. doi:10.1111/j.1365-246x.2008.03768.x
- Sirgue, L., and Pratt, R. G. (2004). Efficient Waveform Inversion and Imaging: A Strategy for Selecting Temporal Frequencies. *Geophysics* 69, 231–248. doi:10.1190/1.1649391
- Smith, J. D., Ross, Z. E., Azizzadenesheli, K., and Muir, J. B. (2022). HypoSVI: Hypocenter Inversion with Stein Variational Inference and Physics Informed Neural Networks. *Geophys. J. Int.* 228, 698–710. doi:10.1093/gji/ggab309
- Song, C., and Alkhalifah, T. (2019). Microseismic Event Estimation Based on an Efficient Wavefield Inversion. *IEEE J. Sel. Top. Appl. Earth Obs. Remote Sens.* 12, 4664–4671. doi:10.1109/jstars.2019.2946903
- Song, C., Alkhalifah, T., and Wu, Z. (2019b). Microseismic Event Estimation and Velocity Analysis Based on a Source-Focusing Function. *Geophysics* 84 (3), KS85–KS94. doi:10.1190/geo2018-0205.1
- Song, C., Wu, Z., and Alkhalifah, T. (2019a). Passive Seismic Event Estimation Using Multi-Scattering Waveform Inversion. *Geophysics* 84, KS59–KS69. doi:10.1190/geo2018-0358.1
- Stanek, F., and Eisner, L. (2013). “New Model Explaining Inverted Source Mechanisms of Microseismic Events Induced by Hydraulic Fracturing,” in 83rd Annual International Meeting, SEG Technical Program Expanded Abstracts 2013, Houston, 2201–2205. doi:10.1190/segam2013-0554.1
- Steinberg, A., Vasyura-Bathke, H., Gaebler, P., Ohrnberger, M., and Ceranna, L. (2021). Estimation of Seismic Moment Tensors Using Variational Inference Machine Learning. *J. Geophys. Res. Solid Earth* 126, e2021JB022685. doi:10.1029/2021jb022685
- Sun, B., and Alkhalifah, T. (2019). A Robust Waveform Inversion Using a Global Comparison of Modeled and Observed Data. *Lead. Edge* 38 (3), 185–192. doi:10.1190/le38030185.1
- Sun, J., Xue, Z., Formel, S., Zhu, T. Y., and Nakata, N. (2016). “Full Waveform Inversion of Passive Seismic Data for Sources and Velocities: 86th Annual International Meeting,” in SEG International Exposition and 86th Annual International Meeting, SEG Technical Program Expanded Abstracts 2016, 1405–1410.
- Tape, C., Liu, Q., Maggi, A., and Tromp, J. (2009). Adjoint Tomography of the Southern California Crust. *Science* 325, 988–992. doi:10.1126/science.1175298
- Tape, C., Liu, Q., Maggi, A., and Tromp, J. (2010). Seismic Tomography of the Southern California Crust Based on Spectral-Element and Adjoint Methods. *Geophys. J. Int.* 180, 433–462. doi:10.1111/j.1365-246x.2009.04429.x
- Tarantola, A. (1984). Inversion of Seismic Reflection Data in the Acoustic Approximation. *Geophysics* 49, 1259–1266. doi:10.1190/1.1441754
- Thurber, C. H. (1992). Hypocenter-velocity Structure Coupling in Local Earthquake Tomography. *Phys. Earth Planet. Interiors* 75, 55–62. doi:10.1016/0031-9201(92)90117-e

- Uchide, T. (2020). Focal Mechanisms of Small Earthquakes beneath the Japanese Islands Based on First-Motion Polarities Picked Using Deep Learning. *Geophys. J. Int.* 223, 1658–1671. doi:10.1093/gji/ggaa401
- van den Ende, M. P., and Ampuero, J. P. (2020). Automated Seismic Source Characterization Using Deep Graph Neural Networks. *Geophys. Res. Lett.* 47, e2020GL088690. doi:10.1029/2020gl088690
- Van Leeuwen, T., and Herrmann, F. J. (2013). Mitigating Local Minima in Full-Waveform Inversion by Expanding the Search Space. *Geophys. J. Int.* 195, 661–667. doi:10.1093/gji/ggt258
- Van Leeuwen, T., and Mulder, W. A. (2010). A Correlation-Based Misfit Criterion for Wave-Equation Traveltime Tomography. *Geophys. J. Int.* 182, 1383–1394. doi:10.1111/j.1365-246x.2010.04681.x
- Virieux, J., and Operto, S. (2009). An Overview of Full-Waveform Inversion in Exploration Geophysics. *Geophysics* 74, WCC1–WCC26. doi:10.1190/1.3238367
- Waldhauser, F., and Ellsworth, W. L. (2000). A Double-Difference Earthquake Location Algorithm: Method and Application to the Northern Hayward Fault, California. *Bull. Seismol. Soc. Am.* 90, 1353–1368. doi:10.1785/0120000006
- Wang, C., Yingst, D., Farmer, P., and Leveille, J. (2016). “Full-waveform Inversion with the Reconstructed Wavefield Method,” in SEG International Exposition and 86th Annual International Meeting, SEG Technical Program Expanded Abstracts 2016, 1237–1241. doi:10.1190/segam2016-13870317.1
- Wang, H., and Alkhalifah, T. (2021). Direct Microseismic Event Location and Characterization from Passive Seismic Data Using Convolutional Neural Networks. *Geophysics* 86, KS109–KS121. doi:10.1190/geo2020-0636.1
- Wang, H., and Alkhalifah, T. (2018). Microseismic Imaging Using a Source Function Independent Full Waveform Inversion Method. *Geophys. J. Int.* 214, 46–57. doi:10.1093/gji/ggy121
- Wang, H., Guo, Q., Alkhalifah, T., and Wu, Z. (2020). Regularized Elastic Passive Equivalent Source Inversion with Full-Waveform Inversion: Application to a Field Monitoring Microseismic Data Set. *Geophysics* 85 (6), KS207–KS219. doi:10.1190/geo2019-0738.1
- Warner, M., and Guasch, L. (2016). Adaptive Waveform Inversion: Theory. *Geophysics* 81, R429–R445. doi:10.1190/geo2015-0387.1
- Warner, M., Ratcliffe, A., Nangoo, T., Morgan, J., Umpleby, A., Shah, N., et al. (2013). Anisotropic 3D Full-Waveform Inversion. *Geophysics* 78, R59–R80. doi:10.1190/geo2012-0338.1
- Willacy, C., van Dedem, E., Minisini, S., Li, J., Blokland, J.-W., Das, I., et al. (2019). Full-waveform Event Location and Moment Tensor Inversion for Induced Seismicity. *Geophysics* 84, KS39–KS57. doi:10.1190/geo2018-0212.1
- Witten, B., and Shragge, J. (2017). Image-domain Velocity Inversion and Event Location for Microseismic Monitoring. *Geophysics* 82 (5), KS71–KS83. doi:10.1190/geo2016-0561.1
- Wu, R.-S., Luo, J., and Wu, B. (2014). Seismic Envelope Inversion and Modulation Signal Model. *Geophysics* 79, WA13–WA24. doi:10.1190/geo2013-0294.1
- Xu, K., Greenhalgh, S. A., and Wang, M. (2006). Comparison of Source-independent Methods of Elastic Waveform Inversion. *Geophysics* 71, R91–R100. doi:10.1190/1.2356256
- Yang, T., and Sava, P. (2013). “3D Image-Domain Wavefield Tomography Using Time-Lag Extended Images,” in 83rd Annual International Meeting, SEG Technical Program Expanded Abstracts 2013, Houston, 4816–4821. doi:10.1190/segam2013-0279.1
- Yang, Y., and Engquist, B. (2018). Analysis of Optimal Transport and Related Misfit Functions in Full-Waveform Inversion. *Geophysics* 83, A7–A12. doi:10.1190/geo2017-0264.1
- Zhang, H., and Thurber, C. H. (2003). Double-difference Tomography: The Method and its Application to the Hayward Fault, California. *Bull. Seismol. Soc. Am.* 93, 1875–1889. doi:10.1785/0120020190
- Zhang, X., Zhang, J., Yuan, C., Liu, S., Chen, Z., and Li, W. (2020). Locating Induced Earthquakes with a Network of Seismic Stations in Oklahoma via a Deep Learning Method. *Sci. Rep.* 10, 1–12. doi:10.1038/s41598-020-58908-5
- Zhang, Y., and Wang, D. (2009). Traveltime Information-Based Wave-Equation Inversion. *Geophysics* 74, WCC27–WCC36. doi:10.1190/1.3243073
- Zhong, Y., and Liu, Y. (2019). Time-domain Acoustic Full-Waveform Inversion Based on Dual-Sensor Seismic Acquisition System. *J. SEISMIC Explor.* 28, 103–120.
- Zhu, L., and Ben-Zion, Y. (2013). Parametrization of General Seismic Potency and Moment Tensors for Source Inversion of Seismic Waveform Data. *Geophys. J. Int.* 194, 839–843. doi:10.1093/gji/ggt137

Conflict of Interest: The authors declare that the research was conducted in the absence of any commercial or financial relationships that could be construed as a potential conflict of interest.

Publisher’s Note: All claims expressed in this article are solely those of the authors and do not necessarily represent those of their affiliated organizations, or those of the publisher, the editors and the reviewers. Any product that may be evaluated in this article, or claim that may be made by its manufacturer, is not guaranteed or endorsed by the publisher.

Copyright © 2022 Hu, Li and Zhang. This is an open-access article distributed under the terms of the Creative Commons Attribution License (CC BY). The use, distribution or reproduction in other forums is permitted, provided the original author(s) and the copyright owner(s) are credited and that the original publication in this journal is cited, in accordance with accepted academic practice. No use, distribution or reproduction is permitted which does not comply with these terms.